Activating Transition Metal Dichalcogenides Monolayers as Efficient Electrocatalysts for Oxygen Reduction Reaction via Single Atom Doping

Shufang Tian and Qing Tang*

School of Chemistry and Chemical Engineering, Chongqing Key Laboratory of Theoretical and Computational Chemistry, Chongqing University, Chongqing 401331, China

*To whom correspondence should be addressed. E-mail: qingtang@cqu.edu.cn

Abstract: Recent studies in 2D transition-metal-dichalcogenides (TMDs) for electrocatalytic applications have mainly concentrated on MoS_2, while the catalytic properties of the majority of other TMDs remain uncovered. This work reveals the activity of sulfur-based ⅣB-ⅦB TMDs in different phase structures for oxygen reduction reaction (ORR). The pristine TMDs are inactive for ORR. The adatom doping with transition metals and non-metal substitutional doping are efficient strategies to modify TMDs. Particularly, Ni or Co doping on 1T-TiS_2, 2H-TiS_2, 1T-ZrS_2, 1T-TaS_2, 1T-NbS_2 and 2H-TaS_2 act as feasible ORR electrocatalysts with overpotential (0.32~0.55 V) comparable to state-of-the-art Pt-based electrocatalysts. While 2H-WS_2, 2H-TaS_2, 2H-TiS_2 and 1T′-WS_2 can be effectively activated by N doping with overpotential of 0.3 ~ 0.75 V. Our predictions show an effective way to modify ORR activity of TMDs by single atom doping, which would be helpful to

provoke future experimental interests of ORR in these systems.

1. **Introduction**

The renewable energy-conversion system, such as metal-air batteries[1,2] and fuel cells,[3,4] has been considered as an effective solution for reducing environmental pollution and alleviating the global demand for energy. To achieve an optimal performance of such energy devices, it is crucial to accelerate the oxygen reduction reaction (ORR), which is largely limited by the sluggish kinetics at the cathode side.[5,6] At present, the precious platinum-based catalysts are the most efficient ORR electrocatalysts with prominent high activity.[7,8] However, the high-cost and shortage of these noble metals and metal oxides hamper the widespread applications.[9] Therefore, the developments of inexpensive and earth-abundant catalysts with high activity for ORR are highly desirable.[10,11]

Particularly, the large specific surface area of two-dimensional (2D) materials has the potential for the catalytic reactions due to more possible active sites on the surface. Among the discovered 2D materials, transition-metal-dichalcogenides (TMDs) have received extensive attentions because of their versatile intriguing properties closely related to the different phases, thickness, strain engineering, doping and defects.[12,13,14,15-18] Enormous recent studies have been dedicated to grope for the applications of TMDs, including usage as electronics,[19-21] optoelectronics,[22] supercapacitors[23,24] and electrocatalysis.[25] The electrocatalytic applications have attracted special attention because of the global demand for green energy resources for our scientific knowledge based society. Among the large family of TMDs, MoS_2 is one of the most widely studied 2D materials, and many recent studies have

confirmed that phase engineering,[26] metal doping[27] and non-metal substitution[28, 29,30-32] on MoS_2 substrate can tune the electronic properties of MoS_2 and improve the catalytic performance. For example, Xiao et al. theoretically proposed 2H-MoS_2 doped with Co/Ni behaves as remarkable electrocatalysts for ORR by effectively activating O_2.[33] Pumera et al. experimentally demonstrated that doping Fe and Mn on MoS_2 can boost the catalytic performance toward ORR.[34] Song et al. successfully achieved ultrathin phosphorus-doped MoS_2 nanosheets, which hold dramatically enhanced catalytic activity for ORR, with an increase of current density up to 7 fold than the pristine form.[32] In addition, the fabricated N-doped MoS_2 by incorporating high concentration of nitrogen atoms into MoS_2 nanosheet under the atmosphere of ammonia exhibits significantly enhanced performance toward hydrogen evolution reaction (HER).[29,30] The N-doped MoS_2 and carbon dots composite also displayed a high Faradaic efficiency and low onset overpotential for CO_2 electroreduction to CO.[31] Noteworthy, most of the recent advances have been focused on the Mo-based TMDs such as MoS_2, the catalytic properties of the majority of TMDs with other metal compositions still remain uncovered. Recently, Sofer et al. explored the catalytic activity of TaS_2 and found that both 2H TaS_2 and 1T TaS_2 show good ORR performance relatively close to that of Pt/C catalyst.[25]

Given by the continuing interest on TMDs for catalytic applications such as ORR, it is important to make a depth profile analysis of the catalytic behaviors of 2D TMDs family and explore effective strategies to modulate the catalytic activities and identify those compositions with fascinating activities to guide experimental

synthesis. In this investigation, we performed systematic density functional theory (DFT) calculations to probe the ORR performance of a series of sulfur-based TMDs (TM= Ti, Zr, Hf, V, Nb, Ta, W, Re, and Pt) in different phase structures (2H, 1T and 1T'). We firstly evaluated the ORR performance of pristine TMDs. It is found that the surface S layers of pristine TMDs are catalytically inactive for ORR, which are limited by the weak O_2 activation and nearly non-bonded *OOH adsorption. Then, we introduced metal doping (Fe, Co, Ni) on the catalyst surfaces, and the metal dopant becomes the active center. The results showed that Ni@1T-TiS_2, Ni@2H-TiS_2, Ni@1T-ZrS_2, Co@2H-TiS_2, Co@1T-TaS_2, Co@1T-TiS_2, Co@1T-NbS_2 and Co@2H-TaS_2 exhibit promising $4e^-$ ORR activity with viable overpotential between 0.32 ~ 0.55 V. In addition, we also studied the non-metal substitutional doping (N, P) at the surface S site. Among the investigated TMDs, the N-doped 2H-WS_2, 2H-TaS_2, 2H-TiS_2 and 1T′-WS_2 are predicted to be effective $4e^-$ ORR catalysts with overpotential of 0.3 ~ 0.75 V. The P-doping, however, all leads to very strong adsorption of oxygen intermediates, which is due to the higher location of the p electronic states of P dopant towards Fermi level that leads to strong interaction with ORR intermediates, and thus are not suitable for usage as ORR catalysts. The remarkable catalytic behaviors of TMDs doped with single metal atom (Co, Ni) or non-metal N predicted by this work would encourage the fabrication of doped TMDs catalysts for ORR.

2. **Computational Details**

The spin-unrestricted density functional theory (DFT) calculations were

preformed within the Dmol^3 code.[35,36] The Perdew–Burke–Ernzerhof (PBE) functional of the generalized gradient approximation (GGA) were employed to describe the exchange-correlation effect.[37] Double numerical plus polarization (DNP) basis set using DFT semi-core pseudopotential (DSPP) was set as the core treatment. The empirical dispersion-corrected density functional theory (DFT-D) was adopted to describe the Van der Waals interaction between the intermediates and electrocatalysts. A conductor-like screening model (COSMO) was adopted to simulate a H_2O solvent environment with a dielectric constant of 78.54.[38-40] The convergence threshold was set within 1×10^{-5} Ha for energy and 0.005 Å for maximal displacement. The real-space global orbital cut-off radius was set as high as 4.6 Å to ensure high-quality results. A rectangular 2 × 3 × 1 supercell of 2H-phase and T (1T- and 1T′-) phase TMD monolayer including 24 S atoms and 12 metal (M) atoms was constructed. The 4 × 3 × 1 Γ-centered k-points was adopted to sample the Brillouin zone, and a vacuum space with 18 Å was set to eliminate the interaction between adjacent images.

The binding energy of metal dopant, denoted as E_b, was defined by the following equation:

$$E_{\mathrm{b}} = E_{\mathrm{total}}(\mathrm{M/substrate}) - E_{\mathrm{bulk}}(\mathrm{M}) - E_{\mathrm{total}}(\mathrm{substrate}) \quad (1)$$

, where E_{total}(M/substrate), E_{bulk}(M), and E_{total}(substrate) are the total energy of metal doped TMDs, the single metal atom (M denotes Fe, Co, Ni) in bulk, and the TMDs substrate, respectively.

In this work, the Gibbs free energy changes (ΔG) for each elementary step of ORR were calculated from the computational hydrogen electrode (CHE) model as

proposed by Nørskov et al.[41] The free energy is defined as $\Delta G = \Delta E + \Delta ZPE - T\Delta S + \Delta G_{pH} + \Delta G_U$, where ΔE, ΔZPE, T and ΔS are the reaction energy change calculated by DFT calculation, difference in zero-point energy, and the entropy difference at 298.15 K, respectively. The entropy of gas phase molecules (H_2O, H_2) were originated from thermodynamic NIST database. The zero-point energy and vibrational entropy of the oxygenated adsorbates were calculated from the vibrational frequencies by quasi-harmonic approximation. The corresponding correction values are provided in Table S9. The ΔG_{pH} and ΔG_U are the changes of free energy caused by variations in the H^+ concentrations and the electrode potential. The value of pH was set as zero. The calculation details of ΔG_{*OOH}, ΔG_{*O}, ΔG_{*OH} as well as the free energy changes of the four elementary steps (ΔG_1, ΔG_2, ΔG_3, ΔG_4) at equilibrium potential (U = 1.23 V) are shown in Supporting Information (SI).

3. Results and Discussion

ORR activity of pristine TMDs

In this work, we explored nine kinds of TMDs (TM= Ti, Zr, Hf, V, Nb, Ta, W, Re, Pt). Based on the coordination mode of metal atoms, the TMDs monolayers can typically have three different phase structures, 2H-, 1T- or 1T′-phase. The metal atoms have trigonal prismatic coordination in 2H-phase and octahedral or distorted octahedral coordination in 1T or 1T' phase. The possibly existed phase structures of different TMDs are presented in Figure 1b. For VS_2, TiS_2, NbS_2 and TaS_2 monolayers, they can have 2H or 1T phase, among which VS_2, NbS_2 and TaS_2 have thermodynamically favored 2H phase, while TiS_2 prefers the thermodynamically more stable 1T phase. The WS_2 can have 2H phase or distorted 1T' phase, where the

2H phase is thermodynamically preferred. Noteworthy, for the monolayers of ZrS_2, HfS_2, PtS_2 and ReS_2, only the 1T or 1T' phase (1T-ZrS_2, 1T-HfS_2, 1T-PtS_2 and 1T′-ReS_2) has been observed in experiment.[42-45] Hence, for these four TMDs, we mainly focus on the existing 1T- and 1T′-phase in this research. It is commonly found that the phase structure plays a key role in determining the properties and appropriate applications of TMDs materials. For example, the thermodynamically stable 2H-MoS_2 is semiconducting that is attractive to electronic devices,[19] while the meta-stable 1T'-MoS_2 is metallic and has great potential in electrocatalysis.[46, 47] To fully explore the potential of TMDs in ORR applications, we need to investigate the activity of various TMDs in different phase structures. In this case, about 14 TMDs structures are investigated, including the 2H phase of TiS_2, VS_2, NbS_2, TaS_2, and WS_2, the 1T phase of TiS_2, ZrS_2, HfS_2, VS_2, NbS_2, TaS_2, and PtS_2, as well as the 1T' phase of WS_2 and ReS_2.

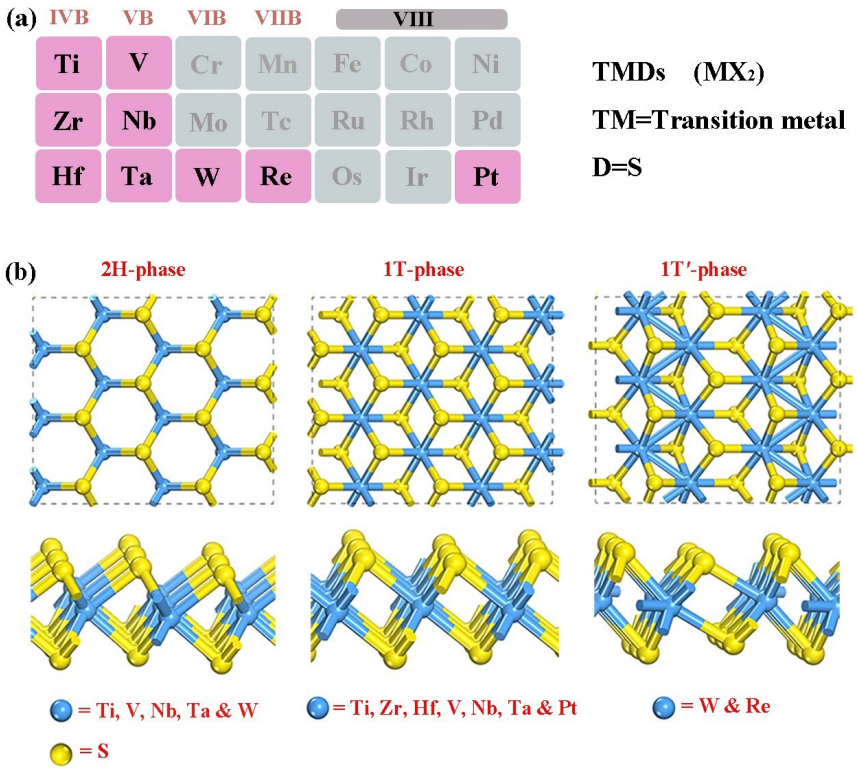

Figure 1. The pink metals represent the TMDs compounds studied in this work (a). Various TMDs exist in different phases (b).

In pristine TMDs, only the basal plane with surface S layer and sandwiched metal layer is accessible, and three possible adsorption sites were tested, including the surface S site, the top of transition metal site and the hollow site. Based on those adsorption sites, we investigated the adsorption behaviors of $*O_2$, *OOH, *O, and *OH intermediates. The results show that all oxygen intermediates prefer to adsorb on the top site of S atom. The Gibbs adsorption free energies (ΔG) of the oxygenated intermediates (ΔG_{*OOH}, ΔG_{*O}, and ΔG_{*OH}) were calculated according to the eqn. 3a-3c (SI) and listed in Table 1.

Table 1. Gibbs adsorption free energy of ORR intermediates on pristine TMDs surface (The unit is eV).

Catalysts	ΔG_{*OOH}	ΔG_{*O}	ΔG_{*OH}	Catalysts	ΔG_{*OOH}	ΔG_{*O}	ΔG_{*OH}
1T-TiS_2	5.24	2.26	1.40	**2H-TiS_2**	5.14	1.45	0.45
1T-VS_2	5.28	1.53	0.82	**2H-VS_2**	5.63	1.99	0.92
1T-NbS_2	5.16	1.97	1.48	**2H-NbS_2**	4.91	1.84	1.01
1T-TaS_2	5.12	1.98	1.57	**2H-TaS_2**	5.28	1.90	1.15
1T′-WS_2	5.19	1.86	1.23	**2H-WS_2**	5.11	2.11	2.51
1T-HfS_2	5.23	2.81	1.77				
1T-ZrS_2	5.35	2.69	1.83				
1T-PtS_2	5.04	1.58	1.90				
1T′-ReS_2	5.67	1.97	1.60				

Herein, the competitive ORR pathways ($4e^-$ vs. $2e^-$) were also investigated. The electroreduction of O_2 can produce either the desired H_2O via four-electron ($4e^-$) pathway or H_2O_2 through the two-electron ($2e^-$) pathway. The difference between them is that *OOH is protonated either by $*OOH + H^+ + e^- \rightarrow *O + H_2O$ ($4e^-$ pathway) or by $*OOH + H^+ + e^- \rightarrow H_2O_2$ ($2e^-$ pathway). The more favorable pathway should have lower potential barrier for *OOH hydrogenation. According to the recent report, if the Gibbs free energy of *O adsorption (ΔG_{*O}) on catalysts is smaller than 3.52 eV ($\Delta G(H_2O_2) - \Delta G(H_2O)$),[48] then the catalyst would prefer $4e^-$ pathway and have high selectivity toward H_2O production. Based on the calculated value of ΔG_{*O} in Table 1, all the investigated 14 catalysts have ΔG_{*O} smaller than 2.69 eV, indicating that they prefer the $4e^-$ pathway to produce H_2O. Hence, we employed the $4e^-$ pathway (R1-R4) (See SI) to evaluate the ORR activity. The change of Gibbs free energy (ΔG) of each elementary reaction step (ΔG_1, ΔG_2, ΔG_3, ΔG_4) under U=1.23V is calculated based on equation 4a-4d in SI, and the results are presented in Table S1.

The theoretical overpotential is thus defined as $\eta_{theo} = \max(\Delta G_1, \Delta G_2, \Delta G_3, \Delta G_4)/e$. Overpotential serves as a useful descriptor to estimate the catalytic performance of ORR. The lower the overpotential, the higher the activity. The predicted overpotential of pristine TMDs is significantly high, from 1.22 V (2H-NbS_2) to 1.98 V (1T′-ReS_2), as shown in Figure S2, which is even larger than the equilibrium electrode potential (1.23V). This indicates that the pristine 2D TMDs are catalytically inactive for ORR. From the calculated values of ΔG_1, ΔG_2, ΔG_3, ΔG_4 (Table S1), one can see that the first elementary step (ΔG_1, O_2 protonated to *OOH) is the rate-determining step, where the adsorption of *OOH intermediate is much weaker than *O and *OH (Table 1). Figure 2 shows the optimized adsorption geometry of O_2 and *OOH over the TMDs surfaces (adsorption geometries of *O and *OH are provided in Figure S1). Clearly, the O_2 molecule is only physically adsorbed with a large separation of more than 3 Å (Figure 2a), where the O-O bond length (1.23 Å) shows negligible changes compared with that of the free O_2 molecule, indicating that it is difficult for pure TMDs to capture and activate oxygen molecule. From Figure 2b, the *OOH is also physically adsorbed and is not bonded to the surface S atom, which indicates that the first-step hydrogenation of O_2 to form *OOH is energetically very unfavorable. Thus one can conclude that the unfavorable O_2 and *OOH binding via the surface S center should be the key for the low activity of pristine TMDs.

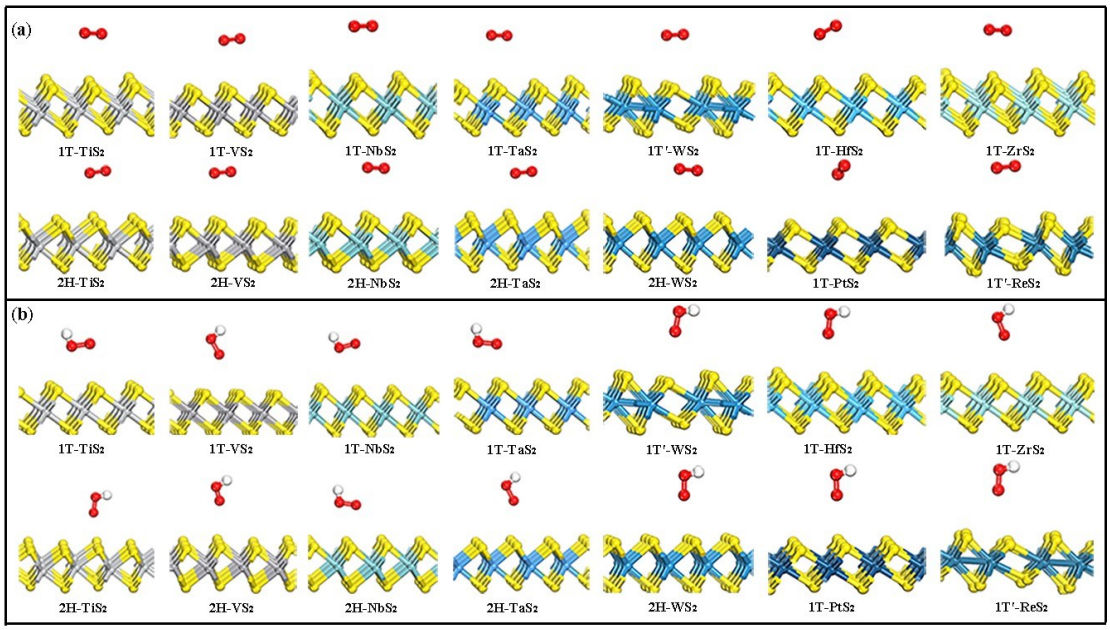

Figure 2. The adsorption configurations of O_2 (a) and *OOH (b) on various TMDs catalysts surface.

On the other hand, from the recent experimental and theoretical researches, doping by metal and non-metal elements can effectively modify and improve the electrocatalytic activity of 2D MoS_2.[28, 29,30-32] Encouraged by these previous studies, we further explored the doping effect on the ORR activity of various TMDs.

ORR activity of transition metal (Fe, Co, Ni) doped on TMDs

We firstly studied the metal doping. Recent experiments have made great progress in achieving isolated single metal atom doping (Fe, Co, Ni, Pt) by covalently bonded to the surface S layer of MoS_2 as adatom.[15, 49-54] Hence we will mainly focus on the adatom doping, and we choose the non-precious and earth abundant metals such as Fe, Co, Ni as the dopant.[55-62] A total of 42 catalysts are constructed by rationally anchoring the single metal atom (Fe, Co, Ni) on the 14 TMDs surfaces. We tested the possible adsorption sites of adatom dopant (Figure 3a). On 2H-phase

surface, there are two possible sites: the hollow site (H) and the top site of sandwiched transition metal element (T_{TM}). On 1T-phase surface, there are also two possible sites: the top site of sublayer S atom (T_S) and the top site of the sandwiched transition metal (T_{TM}). On the 1T'-phase surface, due to the structural distortion, there are two types of S atom: the tensile S atom with three stretched S-M bonds (St) and the compressed S atom with three shortened S-M bonds (Sc). Thus there are three possible adsorption sites on 1T'-phase: the top site of the sandwiched transition metal (T_{TM}), the top site of the sublayer tensile S (T_{St}), and the top site of the sublayer compressed S (T_{Sc}). The test calculations showed that the Fe, Co, Ni dopants prefer to anchor onto the hollow site (H) on 2H-phase, the top site of sublayer S atom (T_S) on 1T-phase, and the top site of the sublayer tensile S (T_{St}) on 1T'-phase, as shown in Figure 3b. Among them, the Fe, Co, Ni not only bond with three neighboring surface S atoms to form three Fe-S (Co-S, Ni-S) bonds, but also bond with three sandwiched TM atoms to form three additional Fe-TM (Co-TM, Ni-TM) bonds. The distance between the metal dopant and the adjacent S atoms ranges from 2.07 to 2.23 Å, and the bond length of doped metal atom with the sandwiched TM atom varies from 2.56 to 2.94 Å.

The aggregation of isolated metal atom on the substrate is a critical concern. Therefore, we need to estimate the stability of metal dopant anchored on 2D TMDs based on the difference between binding energy (E_b, calculated by eqn.1) and metal cohesive energy (E_{coh}). According to the previous report,[63] the energy difference in E_b and E_{coh} (denoted as $\Delta E = E_b - E_{coh}$) < 0.15 eV serves as a benchmark to evaluate the stability of the doped single metal atom. Note that there exists some discrepancy in

the stability criteria set up for single atom catalysts.[63, 64] To establish a proper criteria for the studied 2D TMDs substrates, we then evaluate the stability of Fe-, Co-, and Ni-doped 1T′-MoS_2, which have been successfully synthesized experimentally.[15, 49-54, 65] The calculated energy difference in E_b and E_{coh} for Fe-, Co-, and Ni-doped 1T′-MoS_2 is 0.25 eV, 0.26 eV, and 0.35 eV, respectively (they are more positive than 0.0 eV but can be stably achieved in experiment), thus the criterion of E_b - E_{col} < 0.15 eV (smaller ΔE value than the 1T′-MoS_2 system) could be well-suited to evaluate Fe, Co, and Ni-doped other TMDs compositions. Based on this screening criteria, about 20 out of 42 catalysts are expected to be thermodynamically stable (the catalysts below the red dotted line in Figure 3c), including Fe@2H-NbS_2, Co@2H-NbS_2, Fe@2H-TiS_2, Co@2H-TiS_2, Ni@2H-TiS_2, Co@2H-VS_2, Co@2H-TaS_2, Fe@1T-NbS_2, Co@1T-NbS_2, Ni@1T-NbS_2, Co@1T-TiS_2, Ni@1T-TiS_2, Fe@1T-VS_2, Co@1T-VS_2, Ni@1T-VS_2, Co@1T-TaS_2, Fe@1T-ZrS_2, Co@1T-ZrS_2, Ni@1T-ZrS_2, and Co@1T'-ReS_2. By contrast, substrates such as WS_2 and PtS_2 above the red dotted line are demonstrated as weaker supports to host single metal atom. In addition, we calculated the dissolution potential, $U_{diss} = U^{o}_{diss(metal)} - E_f / ne$, to evaluate the electrochemical stability of screened catalysts, where $U^{o}_{diss(metal)}$ and n denote the standard reduction potential of bulk metal and the number of electrons transferred during dissolution. Usually a positive U_{diss} ($U_{diss} > 0$) can ensure the electrochemical stability of a catalyst system. From Table S2, the U_{diss} for most of the studied M@TMDs is slightly negative except for Fe@1T-VS_2, Co@1T-VS_2 and Ni@1T-VS_2. For comparison, we also calculated U_{diss} of Fe-, Co- and Ni-doped 1T′-MoS_2, which is calculated to be -

1.81 eV, -1.18 eV and -1.07 eV. The Co-doped 1T′-MoS_2 has been experimentally demonstrated to exhibit superior activity and stability for electrocatalytic hydrogen evolution.[27, 65] For other doped TMDs systems with U_{diss} larger than that of Fe, Co, and Ni-doped 1T′-MoS_2, it is anticipated that they can also remain stable under real elctrochemical reaction conditions.

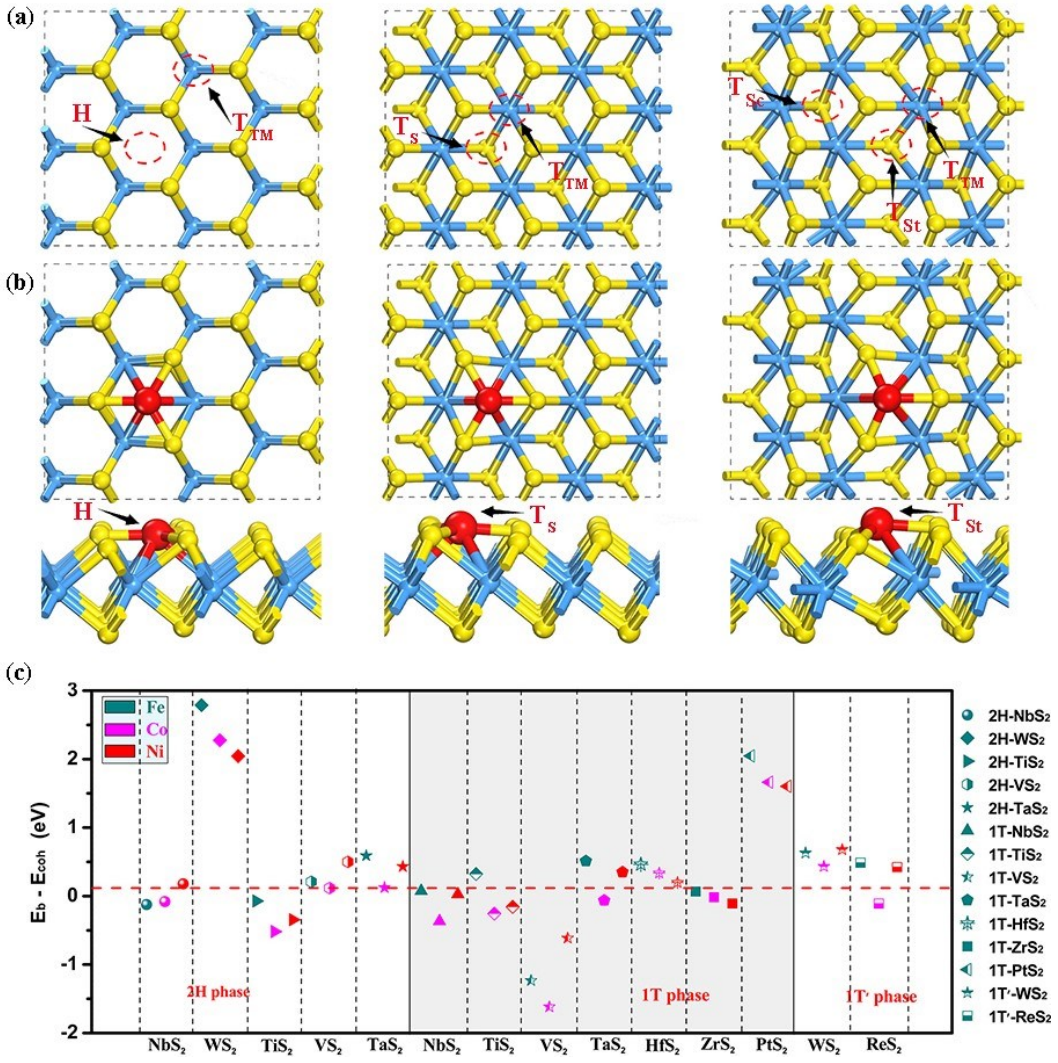

Figure 3. The possible anchoring sites of metal dopant on 2H-, 1T- and 1T′-TMDs (a). The most favorable binding sites of metal dopant on 2H-, 1T- and 1T′-TMDs (top and side view) (b). The energy difference in metal binding energy and cohesive energy (E_b - E_{coh}) of transition metal atom (Fe, Co and Ni) anchored on various TMDs (c).

After estimating the stability of catalysts, only the stable 20 M@TMDs catalysts were further examined for the adsorption of various oxygen species. The O_2 reactant and oxygenated intermediates (*OOH, *O and *OH) all tend to form chemisorption at the M dopant center. The adsorption configurations are depicted in Figure S3. Note that here we mainly focus on the associative mechanism (O_2 reduction to *OOH), while the dissociative mechanism is precluded since the direct O-O cleavage of adsorbed oxygen on the single metal center is energetically very endothermic. The results show that O_2 molecule is chemically adsorbed via side-on or end-on mode on the investigated 20 M@TMDs catalysts. Moreover, in contrast with the non-bonded adsorption of *OOH on pristine TMDs, the M@TMDs all show favorable chemical adsorption of *OOH. Take the 2H-TiS_2 case as an example, the O_2 and *OOH adsorption is very weak on pristine 2H-TiS_2 and the charge transfer between them is negligible (Figure 4a and 4e). After metal doping, we observed substantial charge transfer about 0.49 (0.36), 0.38 (0.31) and 0.17 (0.21) $|e|$ from Fe@2H-TiS_2, Co@2H-TiS_2, and Ni@2H-TiS_2 to the adsorbed O_2 (*OOH), which reveals strong interaction between O_2 (*OOH) and doped 2H-TiS_2 (Figure 4b-d, 4f-h). The calculated Gibbs adsorption free energies of the oxygenated intermediates (ΔG_{*OOH}, ΔG_{*O} and ΔG_{*OH}) are summarized in Figure 5a-c and Table S3. The binding strength of *OOH over M@TMDs is dramatically enhanced by about 1~2 eV than pristine TMDs substrates (Figure 5a). The adsorption of *OH on M@TMDs is also stronger than that of pristine TMDs except for Co and Ni doped 2H-TiS_2 and 1T-VS_2 (Figure 5c). For *O, the TMDs doped by Fe strengthen the bonding strength, while TMDs doped by Co or Ni

weaken the binding with *O except for Co doped 2H-VS_2 (Figure 5b). Hence the metal adatom doping plays a critical role in modulating the binding strength of oxygen and oxygenated intermediates.

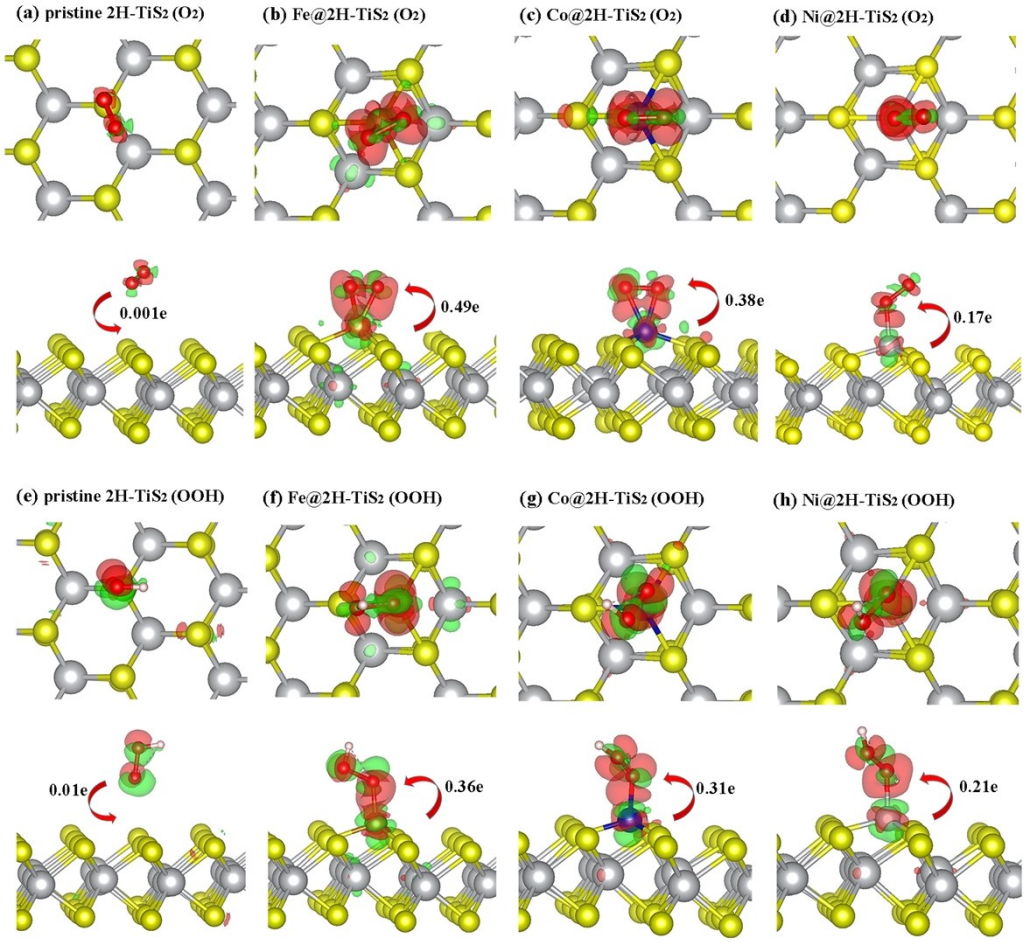

Figure 4. The charge density difference of O_2 and *OOH adsorption on pristine 2H-TiS_2 (a, e), Fe@2H-TiS_2 (b, f), Co@2H-TiS_2 (c, g), and Ni@2H-TiS_2 (d, h). The isosurface level is set as 0.0035 *e* $Å^{-3}$.

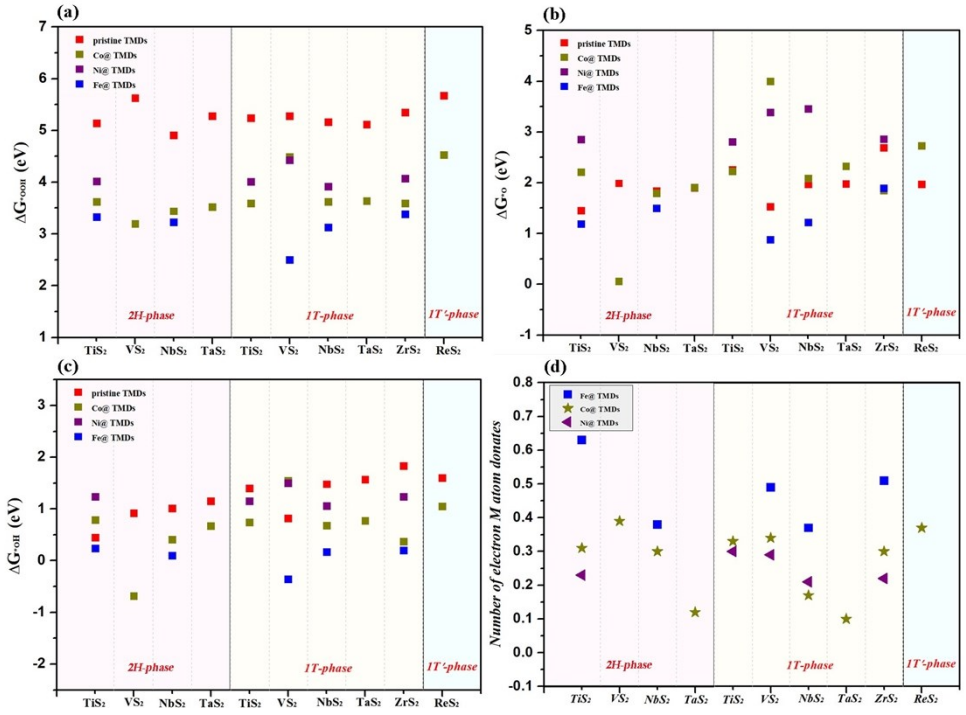

Figure 5. The Gibbs adsorption free energy of *OOH (a), *O (b), *OH (c) on pristine and metal doped TMDs. The number of electron transferred between doped metal atom and TMDs (d).

To explore why the TMDs doped with Fe, Co & Ni enhance the adsorption of most oxygen intermediates, we further analyzed the charge transfer between metal dopant and TMDs (Figure 5d and Table S4). The doped metal atom acts as an electron donor and the number of charge transfer (N_e) varies from 0.10 to 0.63 |e|. One can see that for the same TMDs substrate, the transferred N_e follows a decreasing trend of Fe@TMDs > Co@TMDs > Ni@TMDs. The oxygen intermediate groups are electron-rich and tend to move to the more positive charge center. The larger N_e in Fe@TMDs indicates the Fe center is more positive than Co or Ni. Consequently, the TMDs doped with Fe generally have stronger binding for oxygen intermediates, followed by Co@TMDs and Ni@TMDs. Recently, Sun et al. studied the bond order of oxygen intermediates to Fe^{3+} and Ni^{3+}, and they confirmed the stronger binding

strength at the Fe site in $Ni_xFe_{1-x}OOH$ than the Ni site,[66] which is consistent with our predicted results. In addition, the d-band center as an important descriptor is usually related to the adsorption free energies of oxygen intermediates on transition metal surface. As shown in Figure S4, we calculated the d-band center of transition metal atom doped on TMDs. One can see that the d-band center of Fe is closer to the Fermi level than Co or Ni in the same TMD system. Take 2H-TiS_2 as an example, the d-band center of Fe, Co, and Ni is -1.05 eV, -1.21 eV and -1.68 eV respectively. The higher d-band center down from the Fermi level, the higher resultant anti-bonding level (decreased occupancy) and the stronger adsorption of the oxygenated species, which is consistent with the binding strength of oxygen intermediates: Fe@TMDs > Co@TMDs > Ni@TMDs. The strong bonding on Fe doped systems is detrimental to the ORR performance.

Furthermore, the adsorption free energy of oxygenated intermediates is considered as an important descriptor to estimate the catalytic performance toward ORR.[67] We use ΔG_{*OH} as the descriptor and plot the correlation between the limiting potential (since ΔG in our case is calculated at equilibrium potential of U = 1.23 V, the limiting potential is defined by $U_L = 1.23 - \max(\Delta G_1, \Delta G_2, \Delta G_3, \Delta G_4)/e$) and ΔG_{*OH}, and a volcano-like activity of various M@TMDs catalysts was constructed (Figure 6a). Note that Ni@1T-NbS_2 and Co@1T'-ReS_2 are not located at the volcano curve, since their activity-determining step is determined by the second step (*OOH to *O and H_2O for Ni@1T-NbS_2) or the third step (*O to *OH for Co@1T'-ReS_2), which is different from other M@TMDs systems where the activity is mainly

determined by either the first or the fourth step. From Figure 6a, the smaller the value of ΔG_{*OH}, the stronger the adsorption strength of *OH. The catalysts located at the left branch of the volcano curve bind *OH too strongly. At this point, the limiting step is the fourth step of *OH reduction to H_2O. As the value of ΔG_{*OH} increases, the adsorption strength of *OH gradually weakens, and the overpotential declines as well. When ΔG_{*OH} increases to the intersection of the volcano curve, the overpotential of ORR is the smallest. With the further increase of ΔG_{*OH} (the right branch of volcano curve), the overpotential begins to increase, and the activity-determining step is then determined by the first step (oxygen molecule reduction to *OOH). Hence, the binding strength of *OH ultimately determines the ORR activity, and we can quickly predict the catalytic activity from the volcano plot. Among the examined 20 M@TMDs catalysts, Ni@1T-TiS_2 (limiting potential: 0.91 V), Ni@2H-TiS_2 (0.90 V), Ni@1T-ZrS_2 (0.85 V), Co@2H-TiS_2 (0.79 V), Co@1T-TaS_2 (0.78 V), Co@1T-TiS_2 (0.75 V), Co@1T-NbS_2 (0.69 V) and Co@2H-TaS_2 (0.68 V) are located close to the vertex of the activity volcano curve, which show potentially promising activity for ORR. The calculated ORR energy diagrams of the eight screened ORR catalysts at 0 V and 1.23 V are presented in Figure 6b. From this diagram, the free energy of rate determining step (RDS) can be used to estimate the overpotential. For Ni@1T-TiS_2, Ni@2H-TiS_2 and Ni@1T-ZrS_2, the RDS corresponds to the first step of protonation from $*O_2$ to *OOH with a limiting reaction barrier of 0.32, 0.33, and 0.38 V, respectively. For Co@2H-TiS_2, Co@1T-TaS_2, Co@1T-TiS_2, Co@1T-NbS_2 and Co@2H-TaS_2, the RDS is the last hydrogenation step from *OH to H_2O with a

limiting reaction barrier of 0.44, 0.45, 0.48, 0.54 and 0.55 V, respectively. Note that the predicted overpotential of the eight M@TMDs catalysts (0.32 ~ 0.55 V) is comparable with the Pt-based catalysts (0.4 ~ 0.45 V),[68] indicating that they are highly active for four electron reduction of oxygen to H_2O. Noteworthy, the theoretically predicted ORR overpotential on Pt(111) is 0.55 V, which slightly deviates by about 0.1~0.15 V compared to the experimental value.

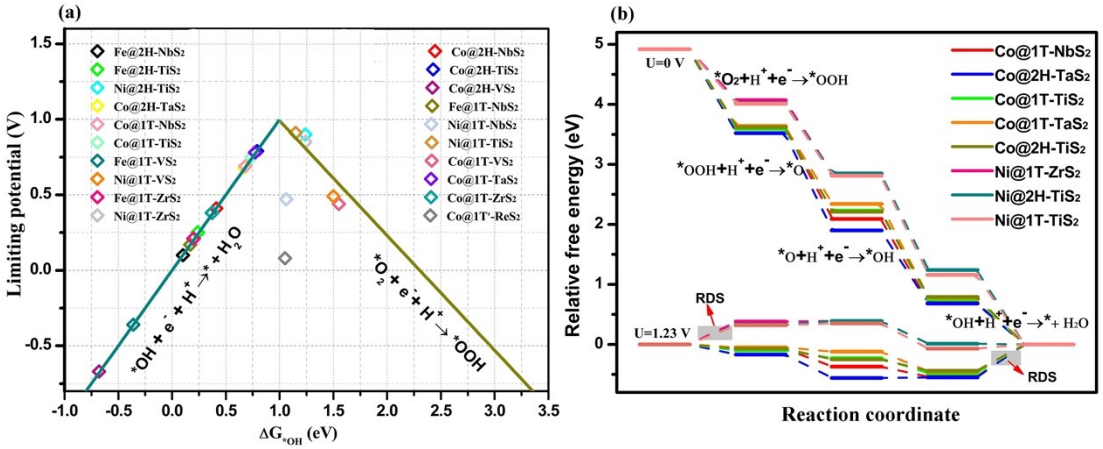

Figure 6. Thermodynamic activity volcano curve of 20 M@TMDs catalysts (a). The free-energy diagram of ORR on screened eight promising catalysts at 0 V and 1.23 V (b).

ORR activity of metal-free heteroatom (N, P) doped on TMDs

Besides metal doping, a large amount of studies have successfully synthesized heteroatom (P and N) substitutional doped MoS_2.[29, 32, 30, 31, 69, 70] These interesting reports arouse our interest to explore the effect of non-metal heteroatom (N/P) substitutional doping on ORR activity of various types TMDs. The geometries of TMDs doped with N and P atom at the S site are shown in Figure S5. It is obvious that the different radius of N and P affect the substitutional doping configurations. The smaller N atom is slightly recessed below surface S layer, while P atom is located on the surface or slightly protruded from the surface. Note that for the 1T′-phase WS_2

and ReS_2, there are two possible doping site. The N and P prefer to dope the compressed S atom (Sc) in 1T′-WS_2, while in 1T′-ReS_2, the stretched tensile S atom (St) is preferred for N doping and the Sc is preferred for P doping. To evaluate the stability of N- and P-doped TMDs, we calculated the formation energy (Ef), which is defined as: $E_{\mathrm{f}} = E_{\mathrm{total}}[\mathrm{doped\ TMD}] - E_{\mathrm{total}}[\mathrm{TMD}] - \mu_S - \mu_X$, where $E_{total}[\mathrm{doped\ TMD}]$, $E_{total}[\mathrm{TMD}]$ are the total energies of the doped and pristine TMD monolayer, respectively, μ_S and μ_X are the chemical potential of S and N (or P) atom. μ_X can be gained from free N_2 and P_4 molecule, and the μ_S can be computed from S_8 molecule. Since the N- and P-doped 2H-MoS_2 have been successfully realized in experiment,[28, 69] the corresponding E_f is calculated for comparison, which is calculated to be 1.98 eV for N/2H-MoS_2 and 1.51 eV for P/2H-MoS_2. From Table S5, most of the studied N- and P-doped TMDs have lower E_f compared with 2H-MoS_2 counterparts, indicating that they have high stability and experimental feasibility. In N-doped TMDs, the O_2 molecule is physically adsorbed, while *OOH, *O and *OH are mostly chemically bonded to the N atom. In the case of P-doped TMDs, the O_2 molecule, *OOH, *O and *OH are all chemically adsorbed (Figure S6). The corresponding Gibbs adsorption free energies (ΔG_{*OOH}, ΔG_{*O} and ΔG_{*OH},) as well as the overpotentials of ORR are calculated and shown in Figure 7 (detailed data are listed in Table S6-S7). For the ideal catalysts, the ΔG_{*OOH}, ΔG_{*O} and ΔG_{*OH} should be 3.69, 2.46, 1.23 eV, respectively.[71] For N-doped TMDs catalysts, ΔG_{*OOH} is mostly greater than 3.69 eV, indicating the slightly weak adsorption of *OOH on catalysts. The adsorption of *O and *OH on the catalyst surface is relatively moderate. Reversely, the *OOH, *O and

*OH species are strongly bound to P-doped TMDs, which is rather difficult for protonation reduction compared with N-doped TMDs. As shown in Figure 7b, the overpotentials of all the P-doped TMDs are higher than the equilibrium potential (U = 1.23 V). This indicates that the substitutional P doping overbinds the oxygenated intermediates, which is ineffective for tuning the ORR activity of TMDs. Among the 14 N-doped TMDs candidates, we screened out four catalysts with promising catalytic activity, including N/2H-WS_2, N/2H-TaS_2, N/2H-TiS_2 and N/1T′-WS_2 with overpotential of 0.35, 0.55, 0.57 and 0.75 V, respectively.

Moreover, since B is also a common dopant, we also studied the feasibility of B heteroatom substitutional doping for ORR. The optimized configurations indicate that the B dopant is slightly recessed on the surface of TMDs substrate due to its small atomic radius (Figure S7). Then, we investigated the adsorption behavior of O_2 on B/TMDs, as shown in Figure S8. It can be clearly seen that B/TMDs are easily oxidized after interaction with oxygen molecule. The B doped TMDs are chemically too reactive and thus not suitable as catalysts for ORR.

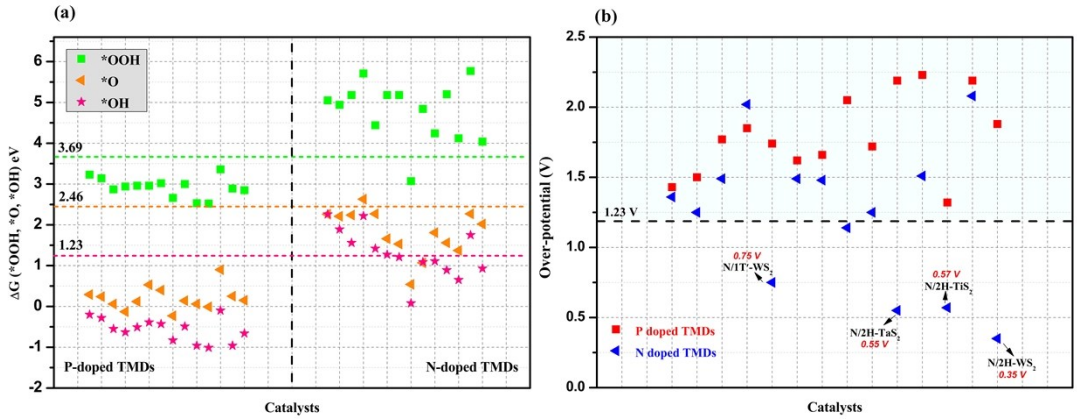

Figure 7. The Gibbs adsorption free energy of *OOH, *O and *OH on N- and P-doped TMDs surface (a). Overpotential of different N- and P-doped TMDs catalysts (b).

We should note that the ORR activity of doped TMDs is mainly depended on the binding strength of oxygenated intermediates. The catalysts with a moderate binding will be more active than that binding too weakly or too strongly. Next, we will explore what causes the difference in adsorption strength of N- and P-doped TMDs. The charge transfer (*Ne*) between N/P dopant and TMDs was calculated as well. The doped metal-free atom serves as an electron acceptor, and the electronegativity of N and P are 3.04 and 2.19, respectively. The greater the electronegativity, the stronger the ability to accept electrons, and vice versa. From Figure 8a and Table S8, one can see that the N dopant gains much greater electrons that that of the P dopant in the same TMDs system. This thus can explain the much weaker binding strength of oxygen intermediates to N-doped TMDs because oxygen intermediates are electron-rich and the N dopant is electrically more negative than P. In addition, we also performed electronic structure analyses for N and P atom which serves as the active center for interacting with oxygen species. As depicted in Figure 8b, we use the highest peak of the active center DOS (E_p) below Fermi level as the electronic descriptor, and found that the E_p of the P atom in all the P-doped TMDs are more closer to the Fermi level than that of the N counterparts. Take the N- and P-doped 2H-WS_2 as an example (Figure S9a and 9b), the E_p of the N- and P-doped 2H-WS_2 are -3.89 eV and -0.68 eV, respectively. When the catalysts interact with oxygen intermediates, the electronic states of the active N or P center are interacting with that of the intermediates, their hybridized energy levels split into the anti-bonding state (σ*) (usually goes across the Fermi level) and the bonding state (σ) (under the Fermi

level), as shown in Figure S9c. The difference of the adsorption strength usually comes from the σ*. For the P-doped 2H-WS_2, the P center has higher E_p location close to Fermi level, the σ* moves higher with a lower occupancy, hence the bonding strength between P-doped 2H-WS_2 and oxygen intermediates is stronger than that of N-doped 2H-WS_2. For all N- and P-doped TMDs, the interaction of P-doped TMDs with oxygen intermediates is stronger than that of N-doped TMDs.

Our predictions here provided useful guideline for the design of high efficient TMDs electrocatalysts for ORR by doping with transition metal or non-metal elements. Among the investigated 14 TMDs structures, 1T-TiS_2, 2H-TiS_2, 1T-ZrS_2, 1T-TaS_2, 1T-NbS_2 and 2H-TaS_2 act as feasible ORR electrocatalysts by Ni or Co doping, while 2H-WS_2, 2H-TaS_2, 2H-TiS_2 and 1T′-WS_2 can be effectively activated by N doping. We believe that these insights will be helpful in guiding the design and discovery of 2D TMDs with high-efficiency electrocatalytic properties for ORR and provoke future experimental investigations of O_2 reduction in these systems.

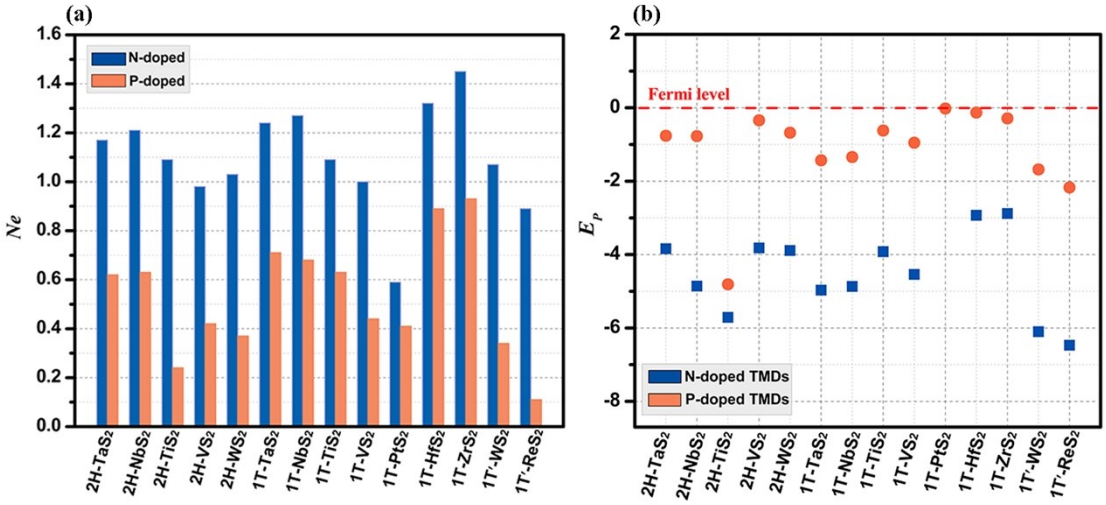

Figure 8. The number of electron transferred (*Ne*) between doped non-metal atom (N and P) and TMDs (a). The highest peak of the active N/P center DOS (E_P) below Fermi level (b).

4. Conclusions

In this fundamental study, the catalytic activities of 14 TMDs with different phase structures have been systematically investigated by using first-principles calculations. All of the pristine TMDs show poor catalytic activity for ORR due to the weak O_2 and *OOH adsorption causing very high barrier and overpotential for the rate-determining step ($*O_2 \rightarrow *OOH$). Then, the introduction of metal adatom doping (Fe, Co, Ni) is considered. The metal dopant acts as the positively charged center, which significantly enhances O_2 adsorption and promotes subsequent hydrogenation reactions. Because of the larger charge transfer, Fe doping tends to induce stronger adsorption of *OOH/*OH than Co or Ni, and eight out of the 42 studied M@TMDs catalysts are screened to be promising in catalyzing ORR with a low overpotential, including Ni@1T-TiS_2, Ni@2H-TiS_2, Ni@1T-ZrS_2, Co@2H-TiS_2, Co@1T-TaS_2, Co@1T-TiS_2, Co@1T-NbS_2 and Co@2H-TaS_2. Moreover, the non-metal substitutional doping is further investigated. The P-doped TMDs with higher location of E_P strongly interact with oxygen intermediates compared with that of N-doped TMDs. Particularly, the excessive binding of P-doped TMDs with *OH makes it difficult for *OH protonation to H_2O with very large over-potential, which show inactivity towards ORR. Fortunately, we find that N-doped 2H-WS_2, 2H-TaS_2, 2H-TiS_2 and 1T′-WS_2 are promising candidates of ORR electrocatalyst. These results show that single atom doping is an effective way to modify ORR intermediates adsorption energies and ORR catalytic activity, which could be useful for future tuning and developing 2D TMDs-based electrocatalysts with high catalytic

performances.

Notes

The authors declare no competing financial interests.

Supporting Information

The calculation details, changes in reaction free energy and Gibbs adsorption free energy of ORR intermediates, the computed dissolution potentials (U_{diss}) for M@TMDs, the zero-point energy (ZPE) and the entropy change (T*S) of doped TMDs, the d-band center, the number of electron transfer, the E_f and E_p of various N/P-doped TMDs, the adsorption configurations of oxygen intermediates and over-potential.

Acknowledgements

This work was supported by the National Natural Science Foundation of China (No.21903008), the Chongqing Municipal Resources and Society Security Bureau (cx2019141), the Chongqing Science and Technology Commission (cstc2020jcyj-msxmX0382), and the Fundamental Research Funds for the Central Universities (2020CDJQY-A031, 2020CDJ-LHZZ-063). This research used resources of the National Supercomputer Center in Guangzhou.

References:

1 Z.-F. Huang, J. Wang, Y. Peng, C.-Y. Jung, A. Fisher, X. Wang, Adv. Energy Mater., 2017, 7, 1700544.

2 M. Wang, T. Qian, S. Liu, J. Zhou, C. Yan, ACS Appl. Mater. Inter., 2017, 9, 21216-21224.

3 Q. Mao, U. Krewer, Electrochim. Acta, 2013, 103, 188-198.

4 K. Mohanraju, L. Cindrella, RSC Adv., 2014, 4, 11939-11947.

5 B. Wang, J. Power Sources, 2005, 152, 1-15.

6 M. Rana, S. Mondal, L. Sahoo, K. Chatterjee, P.E. Karthik, U.K. Gautam, ACS Appl. Mater. Inter., 2018, 10, 33737-33767.

7 Y.H. Lin, X.L. Cui, C.H. Yen, C.M. Wai, Langmuir, 2005, 21, 11474-11479.

8 B. Lim, M. Jiang, P.H.C. Camargo, E.C. Cho, J. Tao, X. Lu, Y. Zhu, Y. Xia, Science, 2009, 324, 1302-1305.

9 F. Cheng, J. Chen, Chem. Soc. Rev., 2012, 41, 2172-2192.

10 A.A. Gewirth, J.A. Varnell, A.M. DiAscro, Chem. Rev., 2018, 118, 2313-2339.

11 J. Li, M. Chen, D.A. Cullen, S. Hwang, M. Wang, B. Li, K. Liu, S. Karakalos, M. Lucero, H. Zhang, C. Lei, H. Xu, G.E. Sterbinsky, Z. Feng, D. Su, K.L. More, G. Wang, Z. Wang, G. Wu, Nat. Catal., 2018, 1, 935-945.

12 H. Li, C. Tsai, A.L. Koh, L. Cai, A.W. Contryman, A.H. Fragapane, J. Zhao, H.S. Han, H.C. Manoharan, F. Abild-Pedersen, J.K. Norskov, X. Zheng, Nat. Mater., 2016, 15, 48-53.

13 X. Wang, Y. Zhang, H. Si, Q. Zhang, J. Wu, L. Gao, X. Wei, Y. Sun, Q. Liao, Z. Zhang, K. Ammarah, L. Gu, Z. Kang, Y. Zhang, J. Am. Chem. Soc., 2020, 142, 4298-

4308.

14 H. Wang, C. Tsai, D. Kong, K. Chan, F. Abild-Pedersen, J.K. Norskov, Y. Cui, Nano Res., 2015, 8, 566-575.

15 Y. Shi, Y. Zhou, D.R. Yang, W.X. Xu, C. Wang, F.B. Wang, J.J. Xu, X.H. Xia, H.Y. Chen, J. Am. Chem. Soc., 2017, 139, 15479-15485.

16 J. Chen, J. Cao, J. Zhou, W. Wang, Y. Zhang, J. Liu, X. Liu, New J. Chem., 2020, 44, 14189-14197.

17 Z. Wang, J. Zhao, Q. Cai, F. Li, J. Mater. Chem. A, 2017, 5, 9842-9851.

18 X. Zhang, S. Shi, T. Gu, L. Li, S. Yu, Phys. Chem. Chem. Phys., 2018, 20, 18184-18191.

19 K. Lee, H.Y. Kim, M. Lotya, J.N. Coleman, G.T. Kim, G.S. Duesberg, Adv. Mater., 2011, 23, 4178-4182.

20 K. Xu, Y. Huang, B. Chen, Y. Xia, W. Lei, Z. Wang, Q. Wang, F. Wang, L. Yin, J. He, Small, 2016, 3106-3111.

21 J. Tang, Z. Wei, Q. Wang, Y. Wang, B. Han, X. Li, B. Huang, M. Liao, J. Liu, N. Li, Y. Zhao, C. Shen, Y. Guo, X. Bai, P. Gao, W. Yang, L. Chen, K. Wu, R. Yang, D. Shi, G. Zhang, Small, 2020, 16, 2004276.

22 W. Wang, X. Zeng, J.H. Warner, Z. Guo, Y. Hu, Y. Zeng, J. Lu, W. Jin, S. Wang, J. Lu, Y. Zeng, Y. Xiao, ACS Appl. Mater. Inter., 2020, 12, 33325-33335.

23 M. Pumera, Z. Sofer, A. Ambrosi, J. Mater. Chem. A, 2014, 2, 8981-8987.

24 X. Peng, L. Peng, C. Wu, Y. Xie, Chem. Soc. Rev., 2014, 43, 3303-3323.

25 J. Luxa, V. Mazanek, M. Pumera, P. Lazar, D. Sedmidubsky, M. Callisti, T.

Polcar, Z. Sofer, Chem-Eur. J., 2017, 23, 8082-8091.

26 S. Bolar, S. Shit, N.C. Murmu, P. Samanta, T. Kuila, ACS Appl. Mater. Inter., 2021, 13, 765-780.

27 K. Qi, X. Cui, L. Gu, S. Yu, X. Fan, M. Luo, S. Xu, N. Li, L. Zheng, Q. Zhang, J. Ma, Y. Gong, F. Lv, K. Wang, H. Huang, W. Zhang, S. Guo, W. Zheng, P. Liu, Nat. Commun., 2019, 10, 5231.

28 A. Azcatl, X. Qin, A. Prakash, C. Zhang, L. Cheng, Q. Wang, N. Lu, M.J. Kim, J. Kim, K. Cho, R. Addou, C.L. Hinkle, J. Appenzeller, R.M. Wallace, Nano Lett., 2016, 16, 5437-5443.

29 Q. Yang, Z. Wang, L. Dong, W. Zhao, Y. Jin, L. Fang, B. Hu, M. Dong, J. Phys. Chem. C, 2019, 123, 10917-10925.

30 Y. Shi, W.-M. Huang, J. Li, Y. Zhou, Z.-Q. Li, Y.-C. Yin, X.-H. Xia, Nat. Commun., 2020, 11, 4558.

31 K. Lv, W. Suo, M. Shao, Y. Zhu, X. Wang, J. Feng, M. Fang, Nano Energy, 2019, 63, 103834.

32 H. Huang, X. Feng, C. Du, W. Song, Chem. Commun., 2015, 51, 7903-7906.

33 B.B. Xiao, P. Zhang, L.P. Han, Z. Wen, Appl. Surf. Sci., 2015, 354, 221-228.

34 V. Urbanova, P. Lazar, N. Antonatos, Z. Sofer, M. Otyepka, M. Pumera, ACS Appl. Mater. Inter., 2020, 12, 20383-20392.

35 B. Delley, J. Chem. Phys., 1990, 92, 508-517.

36 B. Delley, J. Chem. Phys., 2000, 113, 7756-7764.

37 J.P. Perdew, K. Burke, M. Ernzerhof, Phys. Rev. Lett., 1997, 78, 1396-1396.

38 J.A. Keith, G. Jerkiewicz, T. Jacob, ChemPhysChem, 2010, 11, 2779-2794.

39 Y. Sha, T.H. Yu, Y. Liu, B.V. Merinov, W.A. Goddard, III, J. Phys. Chem. Lett., 2010, 1, 856-861.

40 P. Zhang, B.B. Xiao, X.L. Hou, Y.F. Zhu, Q. Jiang, Sci. Rep., 2014, 4, 3821.

41 J.K. Norskov, J. Rossmeisl, A. Logadottir, L. Lindqvist, J.R. Kitchin, T. Bligaard, H. Jonsson, J. Phys. Chem. B, 2004, 108, 17886-17892.

42 M. Zhang, Y. Zhu, X. Wang, Q. Feng, S. Qiao, W. Wen, Y. Chen, M. Cui, J. Zhang, C. Cai, L. Xie, J. Am. Chem. Soc., 2015, 137, 7051-7054.

43 J. Yuan, T. Sun, Z. Hu, W. Yu, W. Ma, K. Zhang, B. Sun, S.P. Lau, Q. Bao, S. Lin, S. Li, ACS Appl. Mater. Inter., 2018, 10, 40614-40622.

44 X. Wang, B. Chen, D. Yan, X. Zhao, C. Wang, E. Liu, N. Zhao, F. He, ACS Appl. Mater. Inter., 2019, 11, 23144-23151.

45 X.R. Nie, B.Q. Sun, H. Zhu, M. Zhang, D.H. Zhao, L. Chen, Q.Q. Sun, D.W. Zhang, ACS Appl. Mater. Inter., 2017, 9, 26996-27003.

46 M.A. Lukowski, A.S. Daniel, F. Meng, A. Forticaux, L. Li, S. Jin, J. Am. Chem. Soc., 2013, 135, 10274-10277.

47 X. Gan, L.Y.S. Lee, K.Y. Wong, T.W. Lo, K.H. Ho, D.Y. Lei, H. Zhao, ACS Appl. Energ. Mater., 2018, 1, 4754-4765.

48 X. Guo, S. Lin, J. Gu, S. Zhang, Z. Chen, S. Huang, ACS Catal., 2019, 9, 11042-11054.

49 K. Qi, X. Cui, L. Gu, S. Yu, X. Fan, M. Luo, S. Xu, N. Li, L. Zheng, Q. Zhang, J. Ma, Y. Gong, F. Lv, K. Wang, H. Huang, W. Zhang, S. Guo, W. Zheng, P. Liu, Nat.

Commun., 2019, 10, 5231.

50 J.-Y. Xue, F.-L. Li, Z.-Y. Zhao, C. Li, C.-Y. Ni, H.-W. Gu, D.J. Young, J.-P. Lang, Inorg. Chem., 2019, 58, 11202-11209.

51 C. Wu, D. Li, S. Ding, Z.U. Rehman, Q. Liu, S. Chen, B. Zhang, L. Song, J. Phys. Chem. Lett., 2019, 10, 6081-6087.

52 G. Liu, A.W. Robertson, M.M.-J. Li, W.C.H. Kuo, M.T. Darby, M.H. Muhieddine, Y.-C. Lin, K. Suenaga, M. Stamatakis, J.H. Warner, S.C.E. Tsang, Nat. Chem., 2017, 9, 810-816.

53 C. Lin, Z. Gao, J. Jin, Chemsuschem, 2019, 12, 457-466.

54 Q. Xiong, Y. Wang, P.-F. Liu, L.-R. Zheng, G. Wang, H.-G. Yang, P.-K. Wong, H. Zhang, H. Zhao, Adv. Mater., 2018, 30, 1801450.

55 J. Chen, F. Zheng, S.-J. Zhang, A. Fisher, Y. Zhou, Z. Wang, Y. Li, B.-B. Xu, J.-T. Li, S.-G. Sun, ACS Catal., 2018, 8, 11342-11351.

56 S. Niu, W.-J. Jiang, Z. Wei, T. Tang, J. Ma, J.-S. Hu, L.-J. Wan, J. Am. Chem. Soc., 2019, 141, 7005-7013.

57 J. Wang, Z. Huang, W. Liu, C. Chang, H. Tang, Z. Li, W. Chen, C. Jia, T. Yao, S. Wei, Y. Wu, Y. Lie, J. Am. Chem. Soc., 2017, 139, 17281-17284.

58 X. Zhao, X. Liu, B. Huang, P. Wang, Y. Pei, J. Mater. Chem. A, 2019, 7, 24583-24593.

59 M. Chen, M. Luo, C. Liu, X. Qi, S.G. Peera, T. Liang, Comput. Theor. Chem., 2020, 1187, 112945.

60 Z. Liang, C. Liu, M. Chen, X. Qi, P.U. Kumar, S.G. Peera, J. Liu, J. He, T. Liang,

New J. Chem., 2019, 43, 19308-19317.

61 Z. Liang, M. Luo, M. Chen, C. Liu, S.G. Peera, X. Qi, J. Liu, U.P. Kumar, T.L.T. Liang, J. Colloid. Interf. Sci., 2020, 568, 54-62.

62 Z. Liang, M. Luo, M. Chen, X. Qi, J. Liu, C. Liu, S.G. Peera, T. Liang, J. Mater. Chem. A, 2020, 8, 20453-20462.

63 C. Ling, L. Shi, Y. Ouyang, X.C. Zeng, J. Wang, Nano Lett., 2017, 17, 5133-5139.

64 X. Lv, W. Wei, B. Huang, Y. Dai, T. Frauenheim, Nano Lett., 2021, 21, 1871-1878.

65 F. Ma, Y. Liang, P. Zhou, F. Tong, Z. Wang, P. Wang, Y. Liu, Y. Dai, Z. Zheng, B. Huang, Mater. Chem. Phys., 2020, 244, 122642.

66 Y. Sun, S. Sun, H. Yang, S. Xi, J. Gracia, Z.J. Xu, Adv. Mater., 2020, 32, 200329.

67 M.T.M. Koper, J. Electroanal. Chem., 2011, 660, 254-260.

68 A. Kulkarni, S. Siahrostami, A. Patel, J.K. Nørskov, Chem. Rev., 2018, 118, 2302-2312.

69 P. Liu, J. Zhu, J. Zhang, P. Xi, K. Tao, D. Gao, D. Xue, ACS Energy Lett., 2017, 2, 745-752.

70 Y. Singh, S. Back, Y. Jung, ChemElectroChem, 2018, 5, 4029–4035.

71 H. Zeng, X. Liu, F. Chen, Z. Chen, X. Fan, W. Lau, ACS Appl. Mater. Inter., 2020, 12, 52549-52559.